JOURNAL OF GEOPHYSICAL RESEARCH, VOL. 104, NO. C5, PAGES 11,471–11,483, MAY 15, 1999

Intercomparison of backscatter maps over Arctic sea ice from NSCAT and the ERS scatterometer

Robert Ezraty and Alain Cavanié

Département d'Océanographie Spatiale, IFREMER, Brest, France

Abstract. C band and Ku band Arctic Ocean sea ice backscatter maps at 40° incidence angle, produced from the ERS 2 active microwave instrument operating in scatterometer mode and Advanced Earth Observing System NASA scatterometers, respectively, are presented and compared. The noise level on these maps is estimated from the comparison of successive maps and is found comparable, although larger at C band than at Ku band. In both cases the relative noise level increases as backscatter level decreases. Backscatter shows a greater dynamic range at Ku band than at C band, going from first-year to multiyear ice; moreover, the Ku band to C band backscatter ratio varies considerably as a function of sea ice type. Surface thawing, in June, leads to a brutal decrease in backscatter in both frequency bands, as well as in the Ku band to C band ratio. The study of the time evolution of backscatter over five different regions of the Arctic Ocean demonstrates the influence of both advection and local evolution on this parameter.

1. Introduction

Sea ice plays an important role in the global climate system and its variability. Not only does it act as an insulating layer between the ocean and the atmosphere, but it also interacts with both media. Modeling and monitoring of the sea ice cover and its modifications in time and space are complementary approaches that benefit from each other. This synergy can be illustrated by the two following examples: Six years of satellite sea ice concentration data have been assimilated into an ice mass balance model [*Thomas et al.*, 1996], and cyclonic and anticyclonic regimes of sea ice displacements have been inferred from a wind-driven model using 47 years of pressure data [*Proshutinsky and Johnson*, 1997]. Such regimes have been later observed using the drift of ice buoys and satellite data in late summers of 1995 and 1996 [*Gohin et al.*, 1997].

Microwave radiometers provide all-weather, all-season imagery of sea ice at polar ocean scale [*Parkinson et al.*, 1987; *Zwally et al.*, 1983] since the early 1970s, with the electronically scanning microwave radiometer (ESMR) on board the Nimbus 5 satellite. It was relayed by the Nimbus 7 scanning multichannel microwave radiometer (SMMR), 1978–1987, whose data were used to map Arctic and Antarctic sea ice [*Gloersen et al.*, 1992]. Since then, the data record has been continuously extended by the special sensor microwave imager (SSM/I) on board the satellites of the Defense Meteorological Satellite Program.

At polar ocean scale, microwave radiometers are well suited for monitoring sea ice extent and sea ice concentration because of the large difference of emissivity (almost a factor of 2) between water and sea ice [*Eppler et al.*, 1992]. The combination of vertical and horizontal polarization brightness temperatures at 19 and 37 GHz permits one to distinguish first-year ice from multiyear ice and to estimate the ice concentration of these two classes [*Cavalieri*, 1992; *Steffen et al.*, 1992]. However, several authors point out that the multiyear concentration, thus obtained, fluctuates during the cold season and is low when compared with the estimation of the previous year [*Comiso*, 1986, 1990; *Thomas*, 1993; *Kwok et al.*, 1996; *Wismann et al.*, 1996]. Monitoring the drift of a large structure, for 2.5 years over the Arctic, *Gohin et al.* [1998] confirmed that sea ice advection could not be invoked to explain this behavior. In this study it was also shown that the backscatter measurements of the active microwave instrument operating in wind mode (AMI-Wind) fluctuate much less than brightness temperatures, thus providing better evidence of sea ice structures.

Since the pioneering work of *Drinkwater and Carsey* [1991] with data from the Seasat scatterometer, much work has been done to clarify the behavior of backscatter over sea ice, as measured from spaceborne scatterometers [*Cavanié and Gohin*, 1992; *Drinkwater et al.*, 1993; *Gohin and Cavanié*, 1994; *Gohin*, 1995; *Gohin et al.*, 1998]. These have large footprint sizes, typically several hundred to several thousand km^2, comparable to those of microwave radiometers. This activity has been encouraged by the free access to high-quality data sets provided by the European Space Agency (ESA) (C band measurements of the AMI-Wind starting in September 1991, presently pursued) and at Ku band by NASA (NASA scatterometer (NSCAT) measurements at Ku band from October 1996 to June 1997).

The objective of the present paper is to compare the possibilities offered by these data sets in the construction of Arctic Ocean backscatter maps over sea ice. Section 2 offers a brief presentation of the methods used to produce these maps. Then, in section 3, different approaches are taken to investigate several aspects of the problem. The relative noise level on the individual maps is evaluated over the Arctic Ocean as a whole and for specific regions. The evolution with time of scatterplots in the C, Ku backscatter space, constructed from all ice-covered pixels over the Arctic Ocean, is presented. Finally, time series of the mean backscatter over selected regions, as well as of the Ku band to C band backscatter ratio are used to illustrate the importance of both advection and local evolution in the observed behavior of backscatter.

Paper number 1998JC900086.
0148-0227/99/1998JC900086$09.00

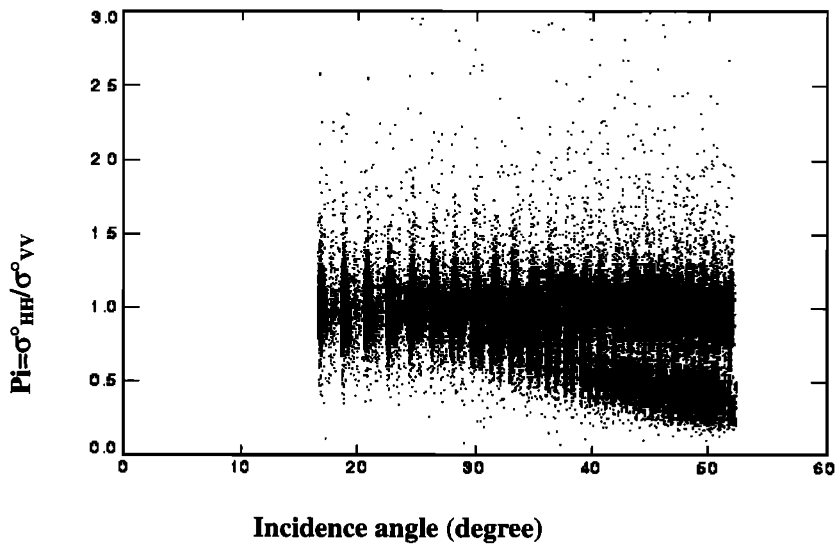

Figure 1. Typical scatterplot of the polarization Index (Pi) as a function of incidence angle over the Arctic Ocean.

2. Sea Ice Backscatter Maps at C and Ku Band Over the Arctic Ocean

The polar stereographic projection used by the National Snow and Ice Data Center (NSIDC) to map sea ice data of past and present passive microwave sensors (ESMR, SMMR, and SSM/I) is convenient for studies at polar ocean scales and has become a standard de facto [*Zwally et al.*, 1983; *Parkinson et al.*, 1987; *NSIDC*, 1992; *Cavalieri et al.*, 1997]. Since 1991, the Centre ERS d'Archivage et de Traitement (CERSAT) has used this projection to produce weekly maps of sea ice backscatter at C band from ESA's AMI-Wind, borne on ERS 1 and ERS 2 satellites. It proved most convenient to use the same projection with a nominal 25 km by 25 km pixel size, practically constant over the Arctic Ocean, to map NSCAT's Ku band backscatter data.

2.1. AMI-Wind Backscatter Maps

The AMI-Wind is a one-swath, three-beam scatterometer in C band (5.3 GHz), VV polarized, and operational on ESA satellites ERS 1 from 1991 to 1996 and ERS 2 from 1996 to the present. The swath begins 225 km from the satellite ground track and is 475 km wide. Because ERS satellites are yaw steered, the three beams always remain 45°, 90°, and 135° to the right of the satellite ground track, so that the fore and aft beams maintain equal incidence angles. The normalized backscatter coefficient delivered by ESA, σ^0, is positioned on a square grid with 25-km spacing, with 19 points across the swath. The individual antenna pulses are recombined using a weighting function that gives the backscatter data an effective 50-km resolution. From the inside to the outside of the track, incidence angles θ vary from 18° to 45° for the central beam and from 25° to 59° for the fore and aft beams. Over the whole range of incidence angles and σ^0, the noise level of σ^0 is nearly constant, around 6%.

In order to produce σ^0 maps at CERSAT, a reference incidence angle of 40° was chosen because it is in the center of the incidence angle range. To relate σ^0 values measured at different incidence angles to a backscatter value at 40°, σ^0_{40}, backscatter in decibels is described as a linear function of incidence angle, with a slope depending on sea ice type [*Gohin and Cavanié*, 1994]. Essentially because the AMI-Wind has only one swath and is at times interrupted by the synthetic aperture radar (SAR) mode operation of the AMI, it proved necessary to use 1 week of data in order to cover the polar oceans as a whole and maintain a reasonable stability of successive backscatter maps. From the backscatter data of the week, the slope, $\partial\sigma^0/\partial\theta$, is computed for each pixel individually and used to relate the individual σ^0 measurements to the backscatter values at 40°, which are then averaged to produce σ^0_{40}.

For these maps, areas of consolidated ice are distinguished from those of open water, pixel by pixel, using a combination of two criteria. The slope, $\partial\sigma^0/\partial\theta$, is required to lie above a given threshold. Furthermore, the absolute value of the ratio of the difference to the sum of the fore and aft beam backscatter measurements is required to be below a second threshold; this is a simple way to apply the criterion that backscatter over large areas of sea ice is essentially isotropic in azimuth [*Cavanié and Gohin*, 1992; *Cavanié et al.*, 1994].

Weekly AMI-Wind backscatter maps as described have been produced for ERS 1 (1991–1996) over both polar oceans and distributed by *CERSAT* [1996]. Their production continues from data of the AMI-Wind on ERS 2. The complete set of maps over both polar oceans is available, as of January 1998, on a World Wide Web server (http://www.ifremer.fr/cersat/ACTIVITE/CEO/IMSI/E_IMSI.ATM). The subset of AMI-Wind and NSCAT maps used in this study can be extracted from this server.

2.2. NSCAT Backscatter Maps

The NASA scatterometer is a dual-swath, Ku band (14 GHz) instrument on board the Advanced Earth Observing System (ADEOS), which flew from August 1996 to June 1997. NSCAT has six antennas (three for each swath), providing observations at three independent azimuths on each side of the satellite. Since the midbeams are dual polarized (VV and HH polarizations), eight independent antenna/polarization combinations are available [*NASA Scatterometer Project*, 1997]. The elementary cell footprint is diamond shaped, 9 km by 32 km.

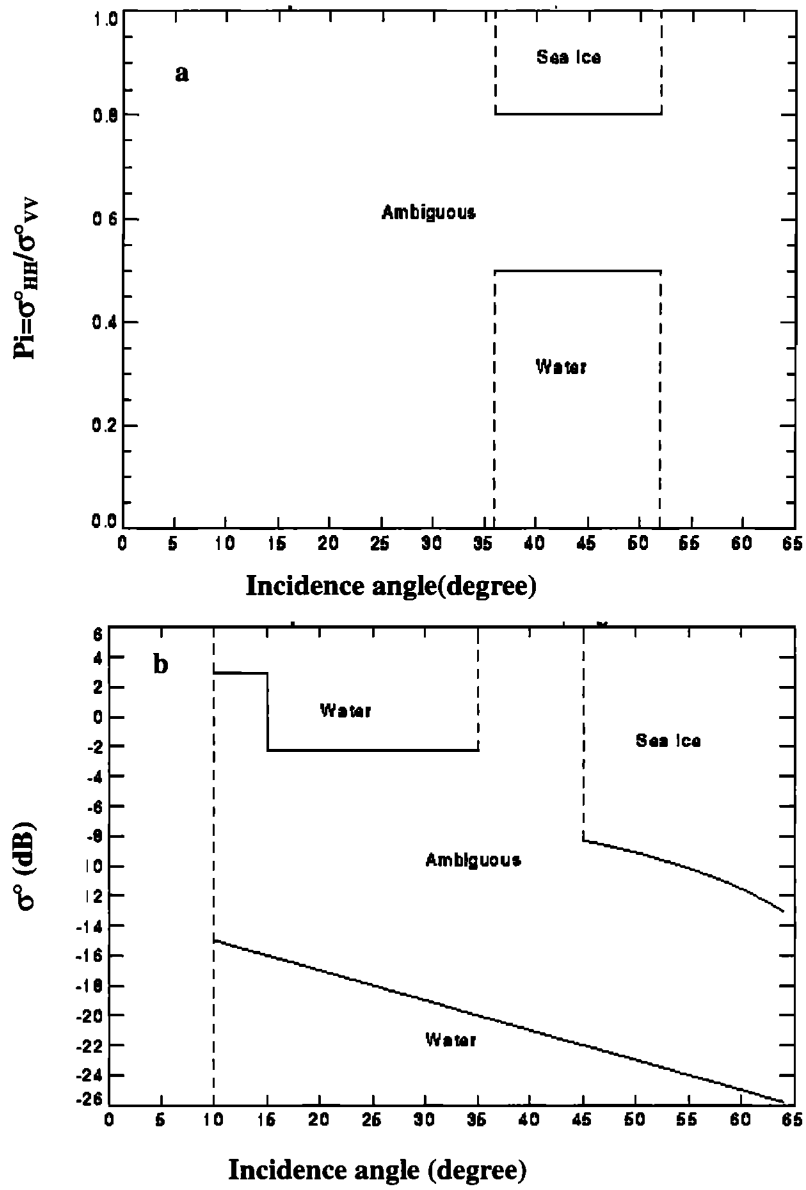

Figure 2. Schematic of the criteria used to discriminate sea ice from open water using NASA scatterometer (NSCAT) data, showing (a) polarization index and (b) backscatter levels as a function of incidence angle.

The incidence angles vary approximately from 17° to 52° and from 21° to 60° for the central and lateral antennas, respectively.

The Physical Oceanography Distributed Active Archive Center (PODACC) provides the level 1.5 data set [*Faist and Lee*, 1996] from which the backscatter maps are produced. This data set contains the individual backscatter measurements over the whole globe [*NASA Scatterometer Project*, 1997]. We restrict and redistribute the individual measurements onto the NSIDC polar grids.

2.2.1. Sea ice/open water discrimination. Since the central antennas of NSCAT provide both VV and HH polarized backscatter values (σ^0_{VV}, σ^0_{HH}), the discrimination between open water and sea ice covered areas is mainly performed through the polarization index (Pi) defined as the ratio of σ^0_{HH} to σ^0_{VV} [*Ezraty and Cavanié*, 1997]. A typical plot of polarization index values as a function of incidence angle θ for a single day and for latitudes higher than 55°N, is presented in Figure 1; to ease visualization, the very few Pi values greater than 3 have been omitted. At incidence angles greater than 30°, the cloud of Pi values splits into two branches; the lower branch corresponds to open water areas, while the upper one, centered around 1, corresponds to sea ice covered areas. Taking into account the inherent measurement noise, two thresholds values have been set for $\theta > 35°$; Pi > 0.8 indicates a sea ice target, while Pi < 0.5 corresponds to open water (Figure 2a). *Yueh et al.* [1997], using Seasat scatterometer data, define a similar parameter, the copol ratio, which is the inverse of our polarization index with upper and lower bounds on σ^0_{HH} and σ^0_{VV}. In regions where the polarization index criterion does not apply or cannot provide a firm discrimination, two other tests are employed [*Ezraty and Cavanié*, 1997]. The first one is based on σ^0 thresholds for selected ranges of incidence angles (Figure 2b); the σ^0 values at 10° incidence angle, although not calibrated (for the NSCAT wind algorithm) are, in this case, used. The second criterion uses an upper bound of the estimate of $\partial\sigma^0/\partial\theta$ at 15° (set to -0.7 degree^{-1}) since, at low incidence

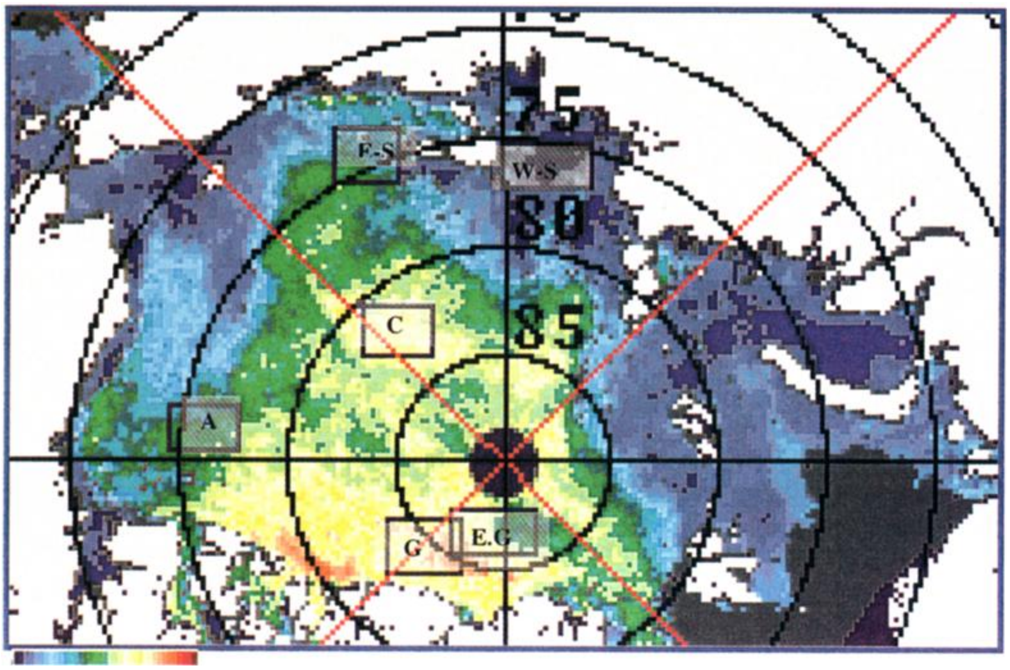

Plate 1. Geographical area and selected sectors. Abbreviations are EG, east Greenland; G, Greenland; C, central Arctic; A, Alaska; ES, east Siberia; and WS, west Siberia. The background is the NASA scatterometer (NSCAT) backscatter map adjusted to 40° incidence angle on March 25–27, 1997, orbits 3152–3195. Open water areas appear as gray.

angles, a steep decrease of σ^0 with θ is typical of open water pixels. Globally, the polarization index criterion is an efficient discriminator of sea ice covered areas while the σ^0 level and the derivative criteria are indicative of open water areas.

2.2.2. Backscatter signature over sea ice at Ku band. Climatological information from previous satellite missions [*Parkinson et al.*, 1987; *Gloersen et al.*, 1992], SSM/I data [*NSIDC*, 1992], and AMI-Wind data [*CERSAT*, 1996] have been used to select areas of different ice types. Six sectors, presented in Plate 1, were chosen as representative of different Arctic regions. The coordinates of the center of these sectors, their areas, and mean backscatter values (AMI-Wind data) are listed in Table 1. The west Siberia sector contains only first-year ice and thus has the lowest mean backscatter value, while the east Siberia sector contains both first- and second-year ice during that winter. All other sectors are formed essentially of multiyear ice. The east Greenland sector was included in the selection because this area corresponds to a maximum in NSCAT backscatter value that persisted during the whole 1996–1997 winter period.

Table 1. Center Coordinates, Areas, and Mean AMI-Wind Backscatter Values $\overline{\sigma^0}$ of the Selected Sectors for March 17–23, 1997

	Latitude, °N	Longitude, deg	Area, km^2	$\overline{\sigma^0}$
Alaska	76.00	142.07 W	93,750	0.0445
Central Arctic	82.14	174.05 E	103,125	0.0759
East Greenland	86.83	55.49 W	112,500	0.0620
Greenland	84.62	90.00 W	120,000	0.0806
East Siberia	74.24	159.51 E	105,000	0.0496
West Siberia	75.97	127.00 E	118,750	0.0184

A sample of the distribution of the backscatter data as a function of incidence angle is presented in Figure 3, where 3 days of data are used in order to cover a wide range of incidence angles. At a given incidence angle a typical range of σ^0 fluctuations would be of the order of 0.1 at 40°, decreasing with θ. Over the whole incidence angle range the second-order polynomial fit to the σ^0 values shows a slight curvature, almost insignificant at incidence angles greater than 25°. It was also observed that the sign of this curvature changed with the sector targeted and, for given sectors, from one antenna to the other. For all sectors, in view of the observed range of σ^0 fluctuations, no significant bias exists between the antennas and between σ^0_{HH} and σ^0_{VV}. Therefore the VV and HH data of all antennas were merged to produce the set of curves presented in Figure 4. These curves were obtained by a second-order least squares polynomial fit over the range $17° < \theta < 60°$. Except for the Greenland sector, which shows an unphysical and unexplained strong negative curvature (backscatter should increase when approaching specular reflection), all curves have a positive curvature, mainly due to the σ^0 data at incidence angles less than 21°. Discarding this range of incidence angles, a linear approximation to the data of each sector is a reasonable fit to the cluster of points. This is a somewhat different approach from a linear fit in decibels, as usually proposed at Ku band [*Drinkwater and Carsey*, 1991; *Yueh et al.*, 1997].

2.2.3. Construction of backscatter maps at 40° incidence angle. NSCAT backscatter maps at 40° incidence angle are constructed using the data of successive 3-day periods. This allows almost every pixel of the NSIDC grid located north of a

b

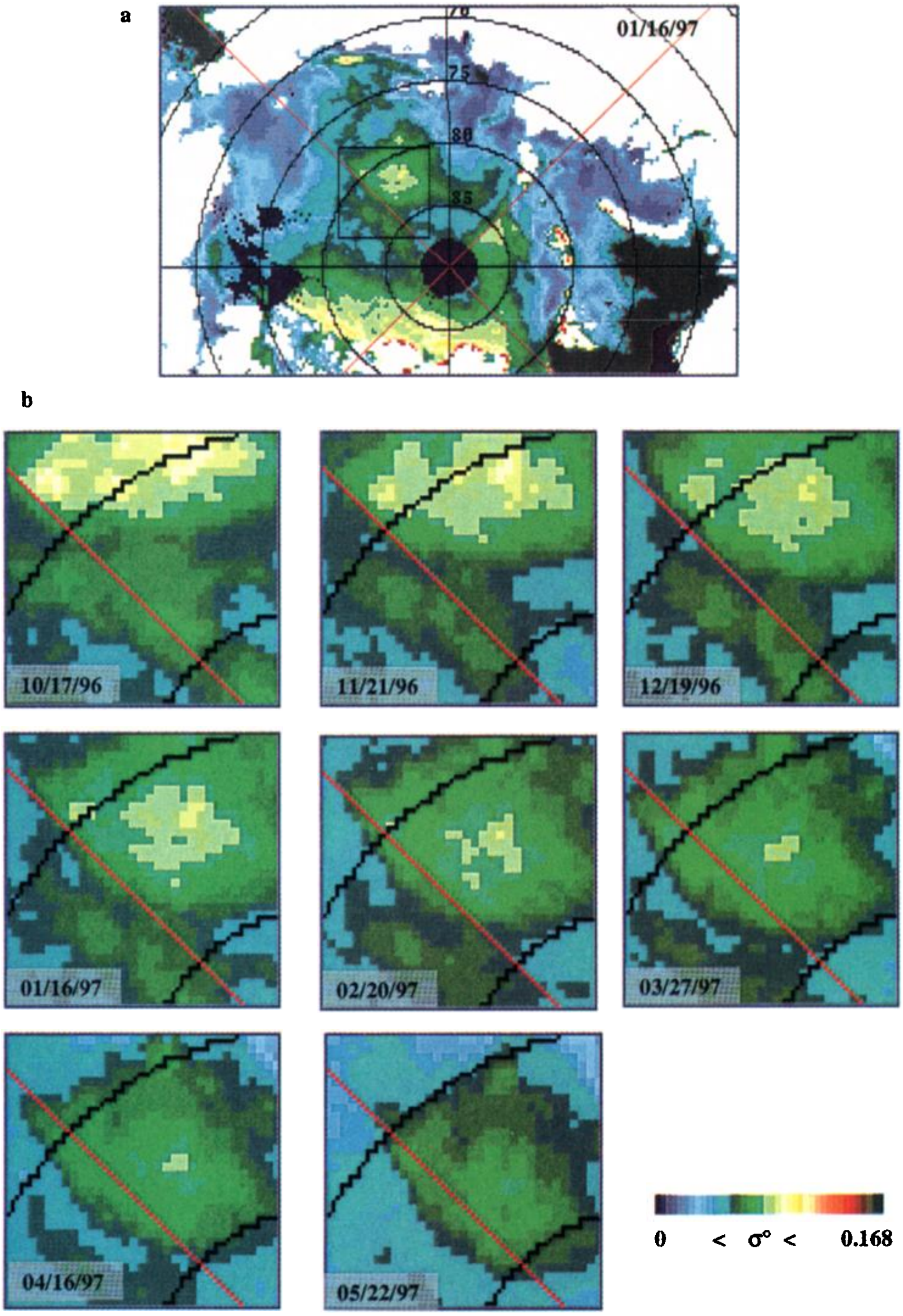

Plate 2. Weekly active microwave instrument operating in wind mode (AMI-Wind) backscatter map at 40° incidence angle centered on January 16, 1997, showing (a) the area studied, with the square indicating the area zoomed, and (b) time series of the zooms from October 17, 1996, to May 22, 1997.

55°N to be sampled more than 10 times, over a wide range of incidence angles.

Sea ice covered regions are first determined within the area defined monthly, from climatological data, for the AMI-Wind processing [*CERSAT*, 1996]. The polarization index and σ^0 level criteria are applied orbit by orbit to distinguish sea ice from open water. For each pixel, discarding data at incidence angles less than 21°, a least squares linear fit to the set of measured backscatter values, $\sigma^0_{\theta,i}$, as a function of θ_i, is computed, with each measurement being weighted by the inverse of its relative noise Kp_i. Backscatter data with Kp values greater than 0.4 are also discarded. The Kp values, provided in the data set, include a nearly constant term related to the wind vector retrieval algorithm (R. Long, personal communication, 1997). Thus, although backscatter data with excessive noise levels are eliminated, the weights used may not be totally representative of the standard deviation of the noise of individual measurements. For each of the pixels the backscatter value adjusted to 40°, σ^0_{40}, is then computed from the coefficients of the linear fit. In the following sections, only σ^0_{40} values are used for both NSCAT and AMI-Wind, thus the subscript 40 will be omitted.

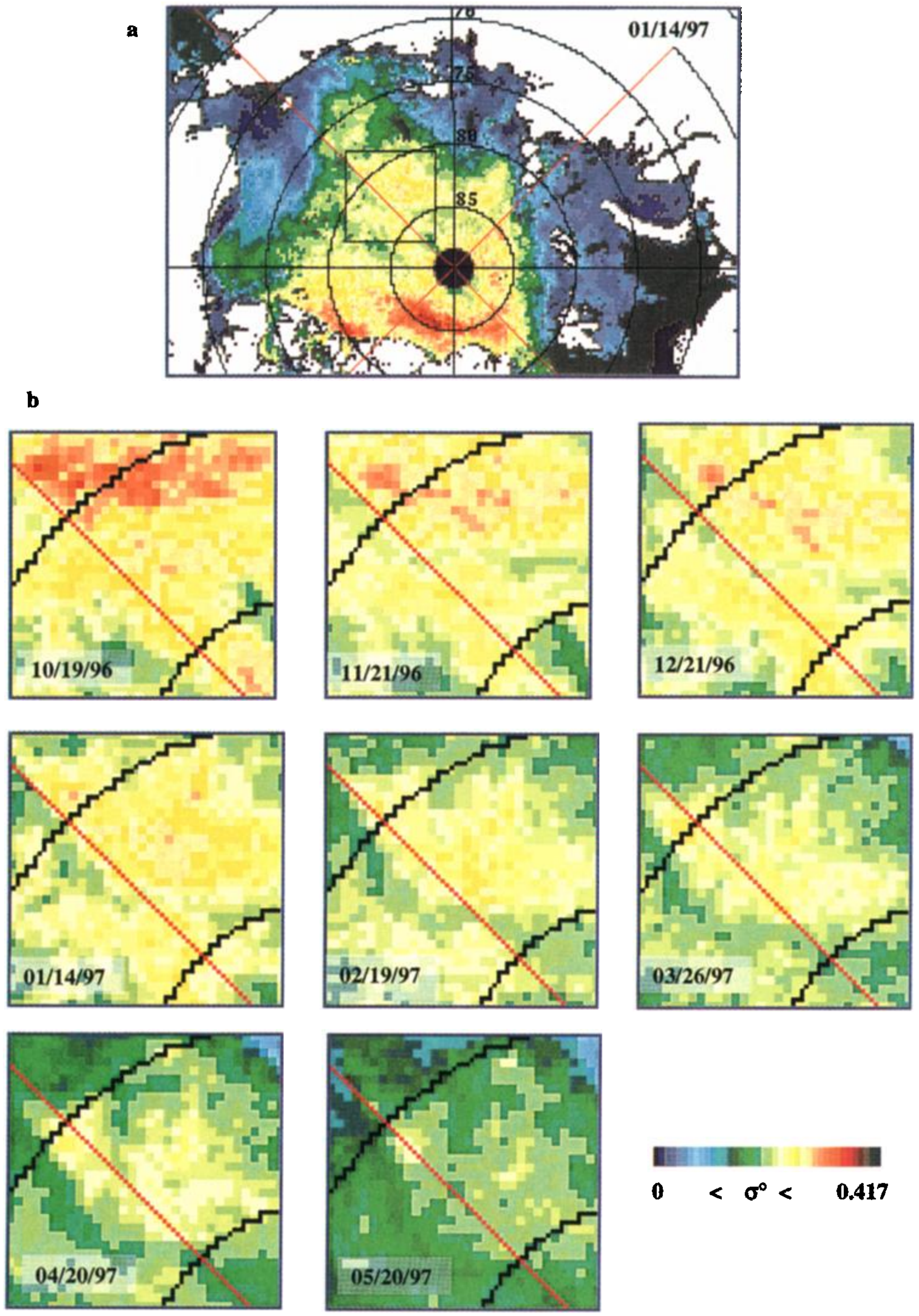

Plate 3. Three-day NSCAT backscatter map at 40° incidence angle centered on January 14, 1997, showing (a) the area studied and (b) time series of the zooms from October 19, 1996, to May 20, 1997.

3. Comparison of NSCAT and AMI-Wind Maps

In sections 3.1 and 3.2 the Ku and C band maps used correspond to the end of the winter period (March 17–30 for the AMI-Wind, March 27 to April 1 for NSCAT), at the time of the year when open water areas in the ice pack are of negligible importance. The evolution of NSCAT and AMI-Wind backscatter signatures during the whole ADEOS lifetime is compared in section 3.3.

3.1. Comparison of Mean Backscatter Values

Each sector is characterized by the average value of the σ^0 of its pixels, $\overline{\sigma^0}$, and by the standard deviation of σ^0, Std(σ^0), divided by $\overline{\sigma^0}$. Table 2 presents these parameters and the ratio of mean Ku band to mean C band backscatter ($\overline{\sigma^0_N}$ and $\overline{\sigma^0_A}$, respectively) for the selected sectors as well as for the ice-covered Arctic as a whole.

The $\overline{\sigma^0}$ values vary similarly for both frequency bands, the lowest values corresponding to the west Siberia sector, the highest to the Greenland sector. The range of variations of $\overline{\sigma^0_N}$ is of the order of 10, while that of $\overline{\sigma^0_A}$ is only of the order of 4, indicating that Ku band is more sensitive than C band to ice type variations. Moreover, it is to be noted that the ratio $\overline{\sigma^0_N}/\overline{\sigma^0_A}$ is not a constant, but it varies from 1.5 for first-year ice to 3.8 for multiyear ice. As expected, since the central sector

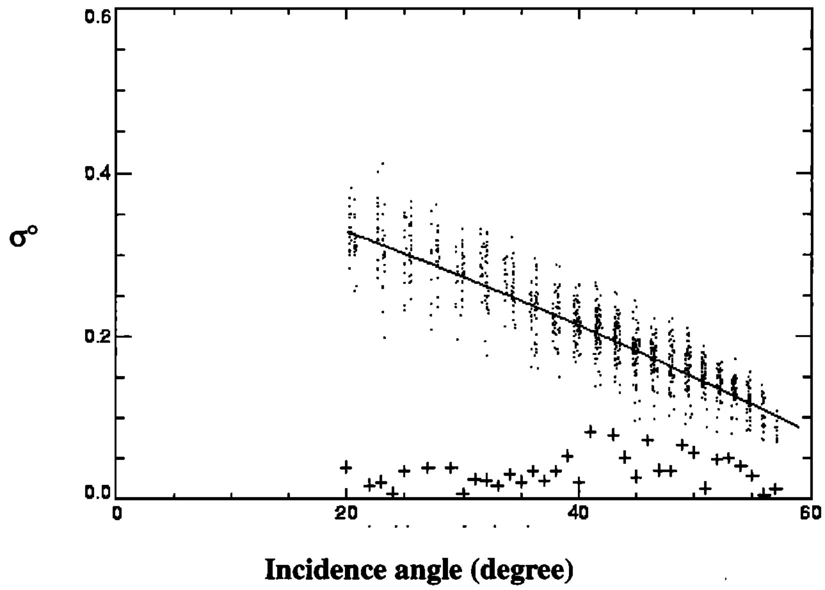

Figure 3. Typical distribution of backscatter data as a function of incidence angle for a single beam and over a selected area. Case presented is from the Alaska sector, beam 2, October 14–16, 1996. The number of data points (pluses) is divided by 1000.

was selected because of its homogeneous backscatter, the ratio $\mathrm{Std}(\sigma^0)/\overline{\sigma^0}$ is lowest there, around 5%. The highest values of this ratio are reached in the west Siberia sector, around 35%, which can be attributed to the important geographical variations of low backscatter in this sector.

3.2. Estimation of the Relative Noise of the Maps

Given two consecutive maps of backscatter at 40° incidence angle, identified by indices 1 and 2, we define for a given pixel, identified by the index i, the relative difference r_i to be the ratio of the difference to the mean of the two successive backscatter values.

$$r_i = (\sigma^0_{1,i} - \sigma^0_{2,i})/[(\sigma^0_{1,i} + \sigma^0_{2,i})/2] \quad (1)$$

Figures 5a and 5b present scatterplots of r_i as a function of the mean backscatter for all ice-covered pixels, for AMI-Wind and NSCAT, respectively. It is clear that for both instruments the relative difference decreases as mean backscatter increases. This may be due to either the behavior of the instrumental noise or to a more rapid evolution in time of backscatter values for sectors of low backscatter.

The variance Π^2 and standard deviation Π of the relative difference of pixel values of two consecutive maps are estimated experimentally using the following:

$$\Pi^2 = \sum_{i=1}^{i=p} r_i^2/p \quad (2)$$

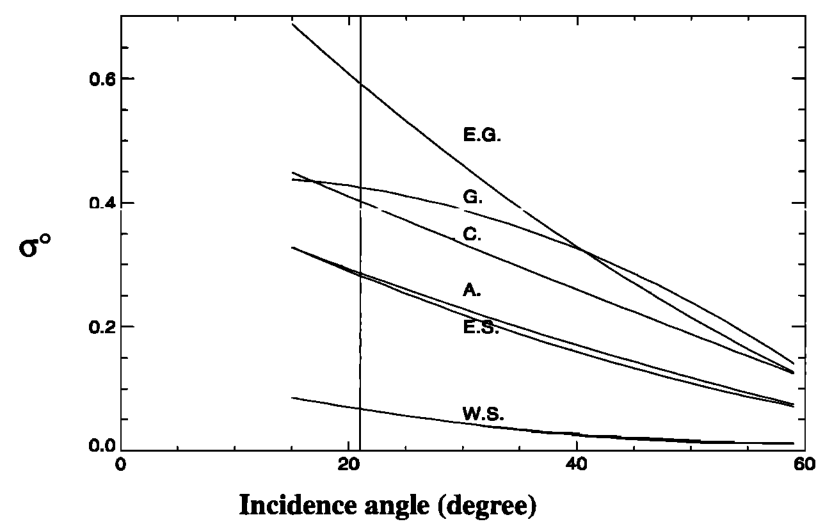

Figure 4. NSCAT backscatter over sea ice as a function of incidence angle for the six selected sectors: EG, east Greenland; G, Greenland; C, central Arctic; A, Alaska; ES, east Siberia; and WS, west Siberia.

Table 2. Backscatter Parameters at Ku and C Band for Selected Sectors

	$\overline{\sigma^0}$		$\mathrm{Std}(\sigma^0)/\overline{\sigma^0}$		
	NSCAT	AMI-Wind	NSCAT	AMI-Wind	$\overline{\sigma_N^0}/\overline{\sigma_A^0}$
Alaska	0.1685	0.0445	0.148	0.112	3.8
Central	0.2438	0.0759	0.049	0.062	3.2
Greenland	0.2882	0.0806	0.080	0.080	3.6
East Siberia	0.1388	0.0496	0.218	0.102	2.8
West Siberia	0.0274	0.0184	0.423	0.304	1.5
Global map	0.1284	0.0421	0.695	0.508	3.1

Std is Standard deviation. Subscripts N and A denote NSCAT (Ku band) and AMI-Wind (C band), respectively.

where p is the number of pixels entering in the sum. We define Ξ, given by the following equation, as the estimated relative noise:

$$\Xi \cong \Pi/\sqrt{2} \tag{3}$$

This estimation assumes that the differences observed are due only to instrumental noise, speckle, and varying number and position of individual backscatter measurements entering in the evaluation of the pixel backscatter values. Since long-term effects such as uncorrected instrument drift, ice advection, and backscatter evolution in time are not taken into account, Ξ is actually an upper bound of the estimate of the relative noise of pixel σ^0 values. This estimate is valid only if the noise level is sufficiently low that fluctuations in the denominator of the expression on the right-hand side of (1) are negligible and if the mean value $\bar{r}$ of r_t is small with respect to the value of Π. Table 3 gives the values of $\bar{r}$ and Ξ for both instruments over the five sectors investigated.

The $\bar{r}$ values are small over all sectors. In the worst case (Alaska), taking $\bar{r}$ into account would only decrease by 15% the estimation of Ξ. Moreover, the values of Ξ are indeed small, always less than 9%, and generally much smaller, so that the hypothesis of negligible influence of perturbations in the denominator of (1) appears justified a posteriori. In four of the five sectors studied, $\bar{r}$ increases or decreases similarly in both

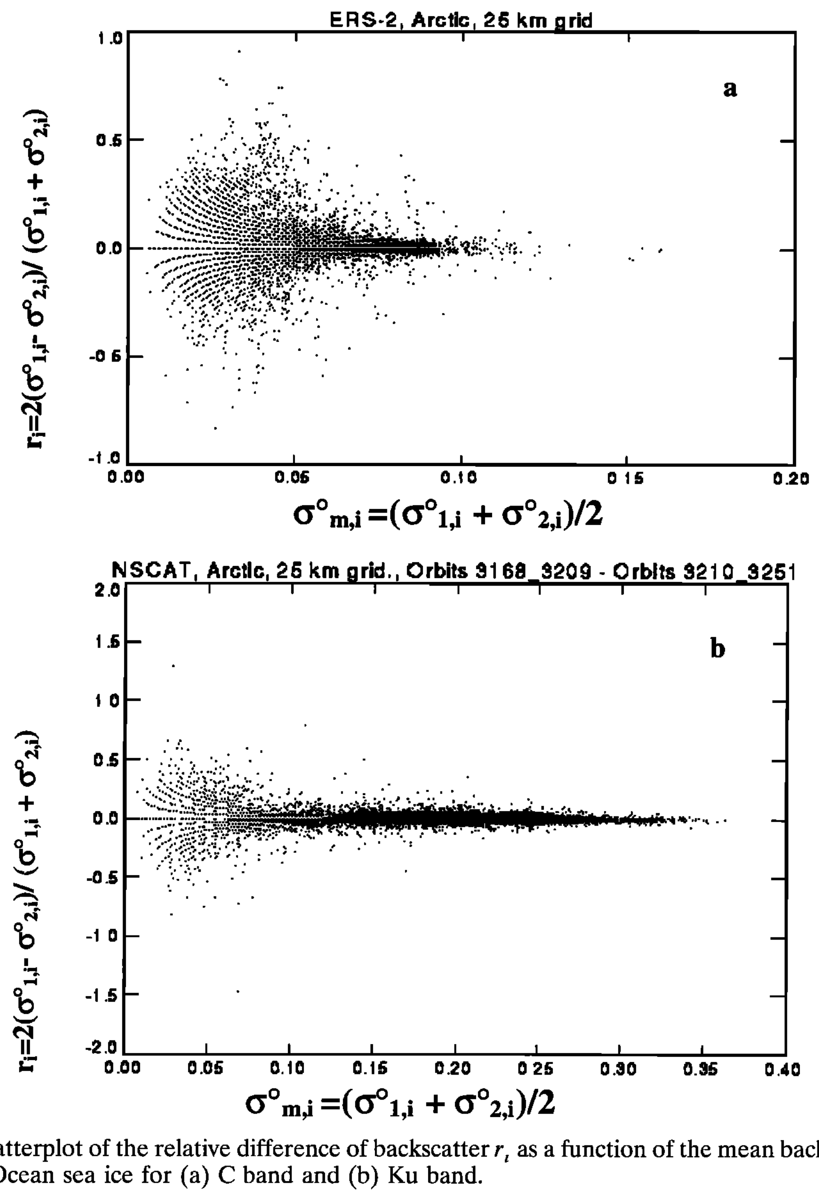

Figure 5. Scatterplot of the relative difference of backscatter r_t as a function of the mean backscatter for the whole Arctic Ocean sea ice for (a) C band and (b) Ku band.

Table 3. Statistics on Relative Noise Levels for AMI-Wind and NSCAT

	AMI-Wind		NSCAT	
	$\bar{r} \times 10^2$	$\Xi \times 10^2$	$\bar{r} \times 10^2$	$\Xi \times 10^2$
Alaska	−3.16	6.32	−0.29	1.65
Central Arctic	1.20	1.53	0.78	1.67
Greenland	0.19	1.90	−0.32	0.98
East Siberia	1.83	3.12	1.26	5.67
West Siberia	3.29	8.46	2.02	4.38

Here $\bar{r}$ is the average of the ratio of relative differences to the mean of two successive backscatter values, and Ξ is relative noise.

frequency bands. This might suggest that a physical phenomenon is involved, the time evolution of the backscatter being a reasonable candidate. However, very low instrument instability, of the order of 0.1 dB (2.3%), could also explain this behavior.

Figure 6 shows the value of Ξ as a function of Ku band backscatter σ_N^0 for the five sectors studied. The dashed curve at Ku band was determined from subsets of points lying in successive backscatter intervals of 0.05. From the similar C band curve the relative errors corresponding to the values of $\overline{\sigma_A^0}$ of the five sectors were determined. These relative errors were then plotted in Figure 6, using the $\overline{\sigma_N^0/\sigma_A^0}$ values of Table 2 to position them on the σ_N^0 axis. In general, the estimated relative noise is higher for the AMI-Wind maps than for those produced from NSCAT data, as previously seen in comparing Figures 5a and 5b. An exception to this is the east Siberia sector, which contains a marked boundary between first- and second-year ice. In this region, subscale fluctuations of the ice may influence the individual NSCAT measurements, whose footprint size is around 200 km^2, while the AMI-Wind integrated footprint size, roughly 12 times greater, must be much less sensitive to the small-scale backscatter variations. Over the Alaska sector the high level of Ξ for AMI-Wind is likely due to switches from SAR mode to AMI-Wind mode. This introduces some spurious data, which cannot be totally discarded when constructing the AMI-Wind maps (F. Gohin, personal communication, 1997).

3.3. Time Evolution of Backscatter

3.3.1. Evolution of backscatter in the C, Ku plane. The time evolution of both C band and Ku band backscatter over sea ice is considered here jointly, over the Arctic Ocean as a whole, using successive σ^0 scatterplots in the C, Ku plane at different times of the year. Comparison of Figure 7a to Figure 7d indicates only a slight evolution of the scatterplots from November to May, during the cold season. However, at the end of June, Figure 7e shows the brutal change in both frequency bands caused by melting and surface ponding.

During the cold season, first-year ice forms a distinct cloud of low backscatter points whose central axis has a slope that corresponds to a ratio $\overline{\sigma_N^0/\sigma_A^0}$ close to 1.2. The low-backscatter portion of this cloud is formed of first-year ice within the consolidated ice pack. The high-backscatter portion corresponds to ice of the marginal zone, essentially located in the Barents Sea. The availability of Ku and C band data serves to distinguish this type of ice from that of the transition zone between first- and second-year ice.

The very old multiyear ice to the north of the Queen Elizabeth Islands and Greenland gives the highest backscatter signatures, both at C and Ku band. A straight line, passed along the upper limit of this region of the scatterplot, has a slope value close to 3. Comparison of the backscatter maps (Plates 2a and 3a) shows that the maximum C band σ^0 values occur close to land while the Ku band σ^0 maximum lies some 200 to 300 km north of the coast. In this region the intensity of melting and puddling decreases rapidly as a function of distance from the coast [*Romanov*, 1995]. These surface phenomena could leave a long-term signature better observed at Ku band than at C band, which penetrates farther into the ice.

The first-year and old multiyear ice region of the scatterplot are linked by a transition zone, ranging from about 0.08 to 0.24

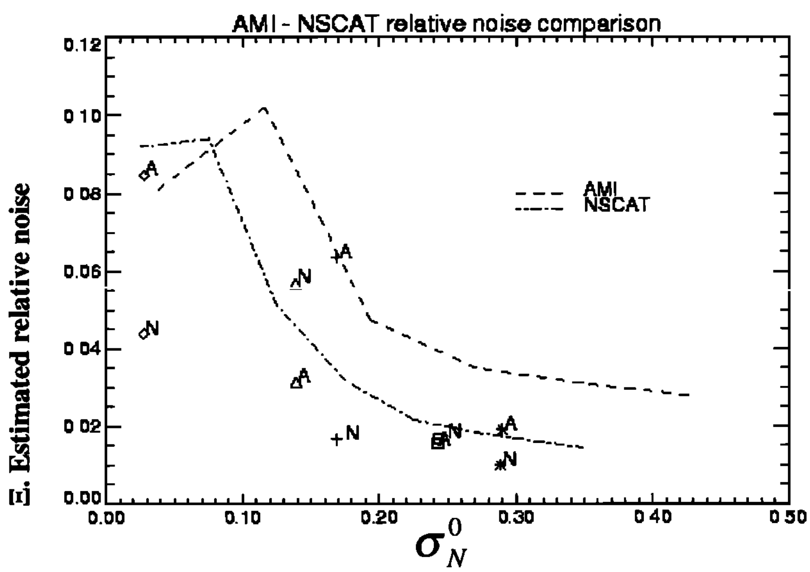

Figure 6. Relative noise of AMI and NSCAT as a function of the Ku band σ^0 for central Arctic (squares), west Siberia (diamonds), east Siberia (triangles), Alaska (pluses), and Greenland (stars). Dashed lines correspond to the whole Arctic Ocean sea ice.

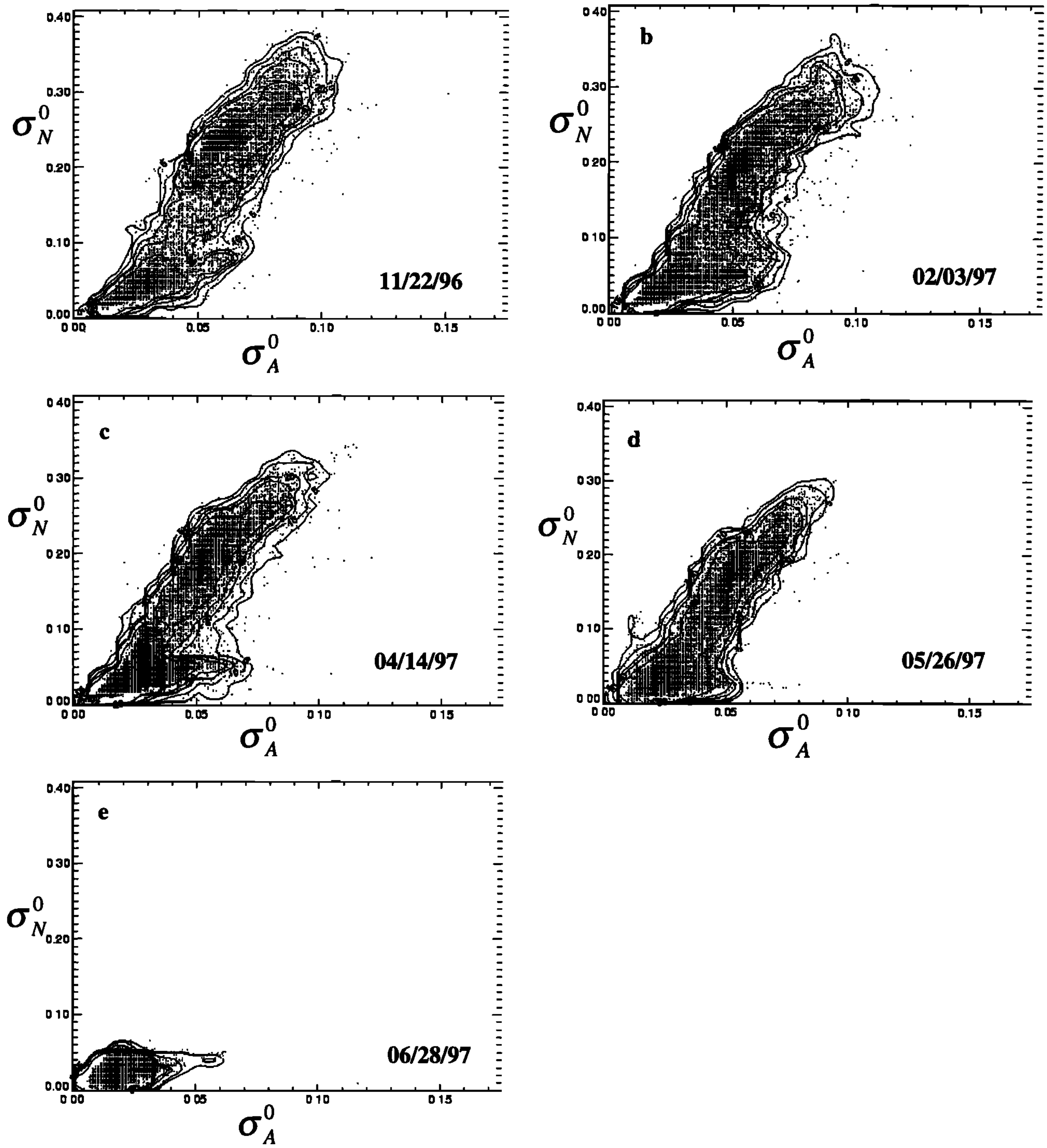

Figure 7. Scatterplots of Ku band versus C band σ^0 over the Arctic Ocean sea ice for (a) November 1996 and (b) February, (c) April, (d) May, and (e) June 1997.

in Ku band σ^0. In this zone the slope of a straight line fit through the data has a value of approximately 6. The transition from first-year to second-year ice has a fairly well defined limit, in the vicinity of 0.08 and 0.03 for Ku and C band values, respectively, of σ^0. However, it is not possible to detect a clear limit between second-year and older ice.

3.3.2. Evolution of backscatter over selected areas. Over the 9-month period of NSCAT data, the evolution as a function of time of backscatter in both frequency bands, averaged over each region individually, differs from one region to the next. To illustrate this, time plots of mean σ^0 are presented, in which C band values are multiplied by a factor of 4, in order to ease the comparison. The time plot for the east Greenland sector (Figure 8), which has the highest backscatter values, shows this factor to be appropriate. The Ku and C band data follow similar curves; a steady decline in backscatter, due to both advection and the local evolution of the ice, occurs from October to mid-June, at which time thawing of the snow and surface ice causes a sudden drop of backscatter.

The curves corresponding to the Greenland, east Siberia,

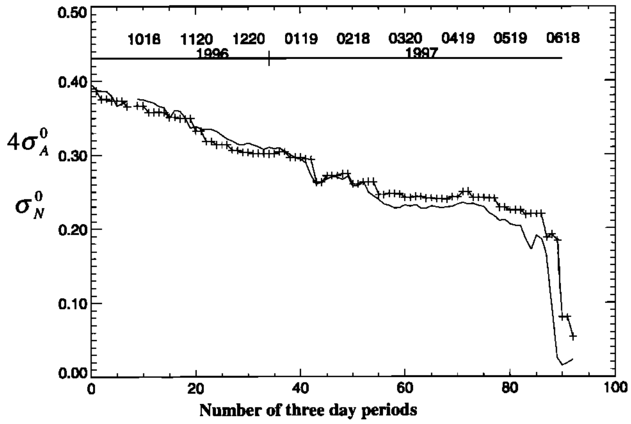

Figure 8. Time series of backscatter values for the east Greenland sector from September 9, 1996, to June 27, 1997. Solid line is Ku band σ^0; pluses denote C band σ^0 multiplied by 4.

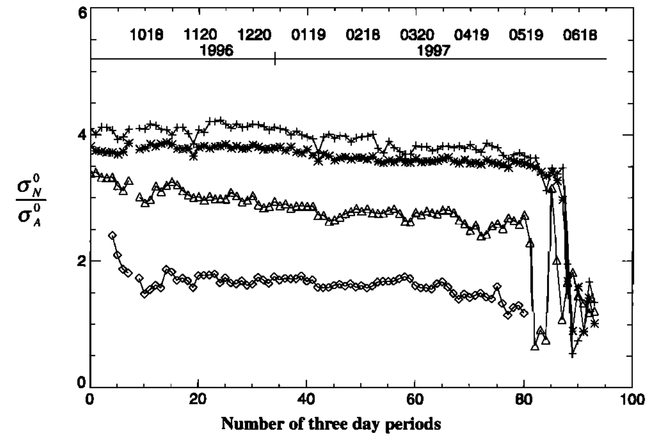

Figure 10. Time series of the ratio of Ku band to C band backscatter values from September 9, 1996, to June 27, 1997, for east Greenland (pluses), Greenland (stars), east Siberia (triangles), and west Siberia (diamonds).

and west Siberia sectors are shown in Figure 9. The Alaska sector is not presented because of numerous data gaps due to SAR operations. For each sector the Ku band curves lie below the corresponding C band curve. From region to region, the ratio σ_N^0/σ_A^0 diminishes as the mean level of backscatter diminishes. On the east Siberia time plot as on the east Greenland time plot, a rapid decrease of backscatter is observed, indicating the onset of thawing, but a cold period refreezes the surface before thawing resumes; the west Siberia curves were intentionally suppressed during this episode, so as to clarify the drawing. In Figures 8 and 9, short-term fluctuations of σ^0 exist in both frequency bands. Both signals are strongly correlated, which indicates that they are not instrumental. An investigation with higher-resolution instruments and at higher sampling rates is required to determine their nature, which is certainly linked to meteorological phenomena.

The time plots of σ_N^0/σ_A^0 (Figure 10) over the four regions whose backscatter time evolution have already been described show this parameter to be more stable than the mean backscatter values. The onset of thawing manifests itself by a rapid decrease of these ratios in all the sectors studied, most likely because attenuation in wet snow is greater at Ku than at C band.

Time plots of backscatter over the central Arctic sector (Figure 11) show a somewhat different behavior than in the other sectors previously studied. Here, from mid-October to the beginning of March, C band σ^0 increases slowly while Ku band σ^0 decreases. Plate 2 and Plate 3 each consist of a backscatter map of the Arctic Ocean as a whole and eight enlargements of a limited zone taken in successive months. This zone is centered on the central Arctic sector and covers an area roughly twice as large and 3 times as high as the sector. The succession of images shows two superposed phenomena: a slow attenuation of mean backscatter with time over the whole region and the advection of an ice feature represented by a backscatter maximum. This feature, roughly 300 km by 700 km in size, progresses northward (to the right and downward on the successive images). It so happens that at Ku band, the effect of attenuation is greater than that of advection, while the opposite is true at C band.

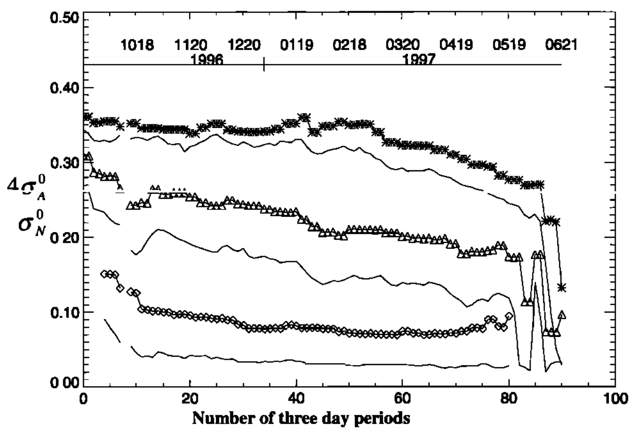

Figure 9. Time series of backscatter values from September 9, 1996, to June 27, 1997. C band σ^0 multiplied by 4 is shown for west Siberia (diamonds), east Siberia (triangles), and Greenland (stars); Ku band σ^0 is shown by solid lines for the corresponding sectors.

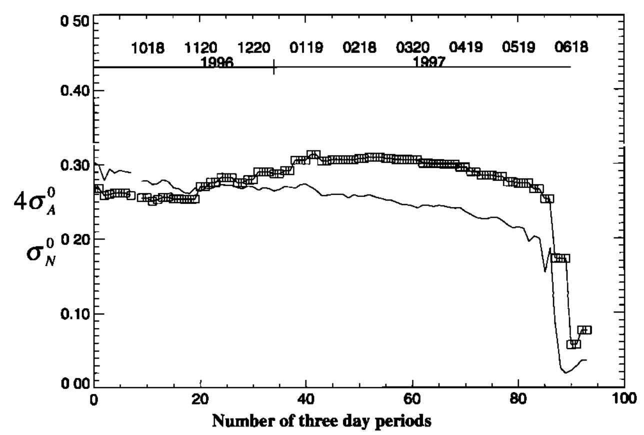

Figure 11. Time series of backscatter values for the central Arctic sector from September 9, 1996, to June 27, 1997. Solid line is Ku band σ^0; squares denote C band σ^0 multiplied by 4.

4. Discussion and Conclusions

In order to monitor sea ice at polar ocean scales using the Ku band data of NSCAT, as has been done since 1991 with the C band data of the AMI in wind mode, a procedure has been developed to produce maps of backscatter at 40° incidence angle. This procedure somewhat differs from that used at C band, the data sets used extending over successive periods of 3 days instead of 7. Moreover, backscatter in linear terms is used throughout, while it is more common to see backscatter in decibels interpolated linearly. The value of the polarization index, the ratio of HH to VV polarized backscatter, which was used to distinguish open water areas, proved to be very close to 1 over sea ice. Thus HH polarized measurements were used, with no specific correction, in conjunction with VV polarized data to produce these maps.

The analysis of successive maps shows that the Ku band maps have a somewhat reduced relative noise level compared to the C band maps. Estimations of the relative noise level of σ^0 measurements have been carried out previously. They employ the isotropy in azimuth of backscatter over sea ice and compare the measurements of the different antennas over the same geographical zone. For the AMI-Wind, unpublished results confirm the 5% to 6% values given by ESA in its level 1.5 products. For NSCAT, in applying the same type of analysis [*Cavanié and Ezraty*, 1997], values range from 6% over regions of high σ^0 to around 15% for regions of low σ^0. Thus it appears that the higher number of individual NSCAT measurements regrouped in individual pixels more than compensates for the higher noise level in the individual measurements. Moreover, the backscatter dynamic range between first-year and multiyear ice is approximately 4 times superior at Ku band than at C band. Thus Ku band maps made with NSCAT data, used individually, are better suited to monitor sea ice in the Arctic than C band maps produced with the AMI-Wind because of their lower noise level, shorter time interval, and greater sensitivity to ice type.

Combining information from both frequency bands is of some interest. The short-term σ^0 fluctuations, observed at both frequency bands in the time series, are strongly correlated; this implies a geophysical origin that would need complementary data sets to be identified. First-year marginal ice and ice interior to the pack, at the limit between first-year and second-year ice, can be distinguished in the C, Ku plane, while this cannot be done using data from a single frequency band. The fact that the backscatter maxima differ notably in geographical position needs further investigation but could also help in ice type identification. The Ku band to C band backscatter ratio is much more stable over a long period of time than the backscatter values in individual frequency bands. This should be helpful to track sea ice in its long-term drift. However, the onset of melt considerably perturbs this parameter, as it does the backscatter measurements in both frequency bands.

QuikScat, then SeaWinds, with their two revolving antennas that maintain constant incidence angles and cover very large swaths, will offer data well adapted to sea ice monitoring at polar ocean scales, since, for large footprints, backscatter over sea ice is isotropic in azimuth. The present work indicates that the 9-month data set of NSCAT, spread over a large range of incidence angles, will prove useful to relate their measurements, limited to two incidence angles, to those of other instruments in C band, such as the AMI-Wind or ESA's next generation of scatterometers, the ASCAT.

Acknowledgments. The authors thank the Centre ERS d'Archivage et de Traitement for processing the backscatter maps from ESA AMI-Wind data and distributing NASA level 1.5 NSCAT data. This study was partially supported by the European Community's Environmental and Climate Program, within the Integrated Use of New Microwave Data for Improved Ice Observation (IMSI) contract.

References

Cavalieri, D. J., Sea ice algorithm, NASA sea ice validation program for the Defense Meteorological Satellite Program Special Microwave Imager: Final report, *NASA Tech. Memo. 104559*, 95 pp., 1992.

Cavalieri, D. J., C. L. Parkinson, P. Gloersen, and H. J. Zwally, Arctic and Antarctic sea ice concentrations from multichannel passive-microwave satellite data sets: October 1978–September 1995, user's guide, *NASA Tech. Memo., 104647*, 1997.

Cavanié, A., and R. Ezraty, Evaluation of Kp on central and lateral antennas of NSCAT over Arctic sea ice, in *Proceedings of the NASA Scatterometer Science Symposium*, pp. 70–72, NSCAT project, Jet Propul. Lab., Pasadena, Calif., 1997.

Cavanié, A., and F. Gohin, Interpretation of ERS-1 scatterometer data over sea-ice, in *ERS-1 Geophysical Validation, Workshop Proceedings, Publ. wpp-36*, pp. 199–201, Eur. Space Agency, Paris, Aug. 1992.

Cavanié, A., F. Gohin, Y. Quilfen, and P. Lecomte, Identification of sea ice zones using the AMI-WIND: Physical bases and applications to the FDP and CERSAT processing chains, in *Proceedings of the Second ERS-1 Symposium, Space at the Service of our Environment, Eur. Space Agency Spec. Publ., ESA SP 361*(2), 1009–1012, 1994.

Centre ERS d'Archivage et de Traitement (CERSAT), Scatterometer Polar Ice Grids User Manual, *Publ. C2-MUT-W-03-IF*, Inst. Fr. de Rech. pour l'Exploit. de la Mer, Brest, France, 1996.

Comiso, J. C., Characteristics of Arctic winter sea ice from satellite multispectral microwave observations, *J. Geophys. Res., 91*, 975–994, 1986.

Comiso, J. C., Arctic multiyear ice classification and summer ice cover using passive microwave satellite data, *J. Geophys. Res., 95*, 13,411–13,422, 1990.

Drinkwater, M. R., and F. D. Carsey, Observations of the late-summer to fall sea ice transition with the 14.6 GHz Seasat scatterometer, paper presented at International Geoscience and Remote Sensing Symposium, IGARSS'91, Inst. of Electr. and Electron. Eng., New York, 1991.

Drinkwater, M. R., D. G. Long, and D. S. Early, Enhanced resolution scatterometer imaging of Southern Ocean sea ice, *ESA J., 17*, 307–322, 1993.

Eppler, D. T., et al., Passive microwave signatures of sea-ice, in *Microwave Remote Sensing of Sea Ice, Geophys. Monogr. Ser.*, vol. 68, edited by F. D. Carsey, pp. 47–69, AGU, Washington, D. C., 1992.

Ezraty, R., and A. Cavanié, Development and evaluation of an NSCAT 25 km resolution sea ice product, *Tech. Rep. DRO/OS 97/03*, Inst. Fr. de Rech. pour l'Exploit. de la Mer, Brest, France, Oct. 1997.

Faist, G., and W. P. Lee, Level 1.5 Data Software Interface Specification (SIS-2), NASA Scatterometer Science Data Processing System, *Publ. JPL D-11788*, revision C, Jet Propul. Lab., Pasadena, Calif., Nov. 1996.

Gloersen, P., W. J. Campbell, D. J. Cavalieri, J. Comiso, C. L. Parkinson, and H. J. Zwally, Arctic and Antarctic sea-ice, 1978–1987: Satellite passive-microwave observations and analysis, *NASA Spec. Publ. SP-511*, 290 pp., 1992.

Gohin F., Some active and passive microwave signatures of Antarctica sea ice from midwinter to spring 1991, *Int. J. Remote Sens., 16*, 2031–2054, 1995.

Gohin, F., and A. Cavanié, A first try at identification of sea ice using the three beam scatterometer of ERS-1, *Int. J. Remote Sens., 15*, 1221–1228, 1994.

Gohin, F., R. Ezraty, and A. Cavanié, 1995, 1996: Two exceptional years illustrating minimum and maximum sea ice extent over the Arctic ocean in late summer, paper presented at Conference on Polar Processes and Global Climate, Arctic Climate System Study, World Meteorol. Organ., Orcas Island, Washington, Nov. 3–6, 1997.

Gohin, F., A. Cavanié, and R. Ezraty, Evolutions of passive and active microwave signatures of a large sea ice feature during its two and half year drift through the Arctic Ocean, *J. Geophys. Res., 103*, 8177–8189, 1998.

Kwok, D., J. C. Comiso, and G. F. Cunningham, Seasonal character-

istics of the perennial ice cover of the Beaufort Sea, *J. Geophys. Res.*, *101*, 28,417–28,439, 1996.
NASA Scatterometer Project, *Science Data Product User's Manual: Overview and Geophysical Data Products*, version 1.1, *Publ. D-12985*, Jet Propul. Lab., Pasadena, Calif., April 1997.
National Snow and Ice Data Center, *DMSP SSM/I Brightness Temperatures Grids for the Polar Regions* (CD-ROM), Boulder, Colo., Jan. 1992.
Parkinson, C. L., J. C. Comiso, H. J. Zwally, D. J. Cavalieri, P. Gloersen, and W. J. Campbell. Arctic sea ice, 1973–1976: Satellite passive microwave observations, *NASA Spec. Publ. SP-489*, 296 pp., 1987.
Proshutinsky, A. Y., and M. A. Johnson, Two circulation regimes of the wind-driven Arctic Ocean, *J. Geophys. Res.*, *102*, 12,493–12,514, 1997.
Romanov, I. P., *Atlas of Ice and Snow of the Arctic Basin and Siberian Shelf Seas*, 2nd ed., Backbone, Elmwood Park, N. J., 1995.
Steffen, K., J. Key, J. Cavalieri, D. J. Comiso, P. Gloersen, K. St Germain, and I. Rubinstein, The estimation of geophysical parameters using passive microwave algorithms, in *Microwave Remote Sensing of Sea Ice, Geophys. Monogr. Ser.*, vol. 68, edited by F. D. Carsey, pp. 201–231, AGU, Washington, D. C., 1992.
Thomas, D., S. Martin, D. Rothrock, and M. Steele, Assimilating satellite concentration data into an Arctic sea ice mass balance model, 1979–1985, *J. Geophys. Res.*, *101*, 20,849–20,868, 1996.
Thomas, D. R., Arctic Sea ice signatures for passive microwave radiometry, *J. Geophys. Res.*, *98*, 10,037–10,052, 1993.
Wismann, V., K. Boehnke, A. Cavanié, R. Ezraty, F. Gohin, D. Hoekman, and I. Woodhouse, Land surface observations using the ERS-1 windscatterometer, II, *Contract 11103/94/NL/CN*, Eur. Space Agency, Paris, 1996.
Yueh, S. H., R. Kwok, S. H. Lou, and W. Y. Tsai, Sea ice identification using dual-polarized Ku-band scatterometer data, *IEEE Trans. Geosci. Remote Sens.*, *33*, 560–569, 1997.
Zwally, H. J., J. C. Comiso, C. L. Parkinson, W. J. Campbell, F. D. Carsey, and P. Gloersen, Antarctic sea ice, 1973–1976: Satellite passive microwave observations, *NASA Spec. Publ. SP-459*, 206 pp., 1983.

A. Cavanié and R. Ezraty, Département d'Océanographie Spatiale, IFREMER, Centre de Brest, BP 70-29280 Plouzane, France. (rezraty@ifremer.fr)

(Received February 16, 1998; revised July 21, 1998; accepted November 16, 1998.)